https://doi.org/10.5194/egusphere-2026-5495
Preprint. Discussion started: 29 September 2026
© Author(s) 2026. CC BY 4.0 License.

Empirical reconstruction of African Humid Periods across the Quaternary

Hang Wang[1], Hu Yang[1], Xiaoxu Shi[1], Jiping Liu[1], Gerrit Lohmann[2], Jiawang Wu[3], Jun Tian[4], Francisco W. Cruz[5], Jianbo Cheng[6], and Dake Chen[1]

[1]School of Atmospheric Sciences, Sun Yat-Sen University and Southern Marine Science and Engineering Guangdong Laboratory (Zhuhai), Zhuhai 519000, China
[2]Alfred Wegener Institute, Helmholtz Centre for Polar and Marine Research, Bremerhaven, Germany
[3]School of Marine Sciences, Sun Yat-Sen University and Southern Marine Science and Engineering Guangdong Laboratory (Zhuhai), Zhuhai, China
[4]State Key Laboratory of Marine Geology, Tongji University, Shanghai, China
[5]Institute of Geosciences, São Paulo University, São Paulo, Brazil
[6]School of Environmental Science and Engineering, Yancheng Institute of Technology, Yancheng, China

Correspondence: Hu Yang (yanghu@sml-zhuhai.cn)

Abstract. As Earth's largest desert, the Sahara experienced periodic humid periods in the geological past, known as African Humid Periods (AHP), which have nurtured the earliest human civilizations. Reconstructing the climatic evolution of the Sahara is therefore important not only for understanding the region's own climate history but also for addressing archaeological questions related to human evolution and migration. Traditionally, the paleoclimate of this region has been reconstructed primarily from geological records, but such reconstructions are costly to obtain and are often subject to considerable chronological uncertainty. Numerical simulations can partly compensate for these limitations but also demand substantial computational resources when reconstructing climate variability over long timescales. To address these challenges, we conducted a series of climate sensitivity experiments to quantify the contributions of different climate forcings, including Earth's orbital, atmospheric CO_2, and ice sheets, to AHP formation. Based on these experiments, we developed a physically based, empirical model that reconstructs the pacing of AHP occurrence using a few key metrics: orbital parameters, CO_2 concentration, and global sea level. We validated this framework against geologic AHP reconstructions spanning the past 800 kilo-years (ka), and further applied it to reconstruct AHP throughout the entire Quaternary. This computationally efficient framework offers a new tool for reconstructing the long-term paleoclimatic evolution of the Sahara, with the potential to refine the chronology of North African geological and archaeological records.

1 Introduction

The Sahara, covering nearly one-third of Africa, is the largest desert on Earth. Yet archaeological (Barth, 1857; Kuper, 1986; Schandelmeier and Thorweihe, 2017) and paleoenvironmental evidence (DeMenocal, 2001; Kuper and Kropelin, 2006; Watrin et al., 2009; Larrasoaña et al., 2013) reveals that this region had repeatedly transformed into a fertile landscape during humid intervals known as the African Humid Periods (AHP). These humid phases, characterized by widespread lakes, rivers,

https://doi.org/10.5194/egusphere-2026-5495
Preprint. Discussion started: 29 September 2026
© Author(s) 2026. CC BY 4.0 License.

and savannas, provided crucial ecological corridors for plants, animals, and human populations (El-Shenawy et al., 2018). However, as the Sahara underwent a return to arid conditions, human civilization in this region was profoundly impacted by the deteriorating living conditions, leading to significant changes in survival strategies (Vernet, 2002) and widespread migrations (Kuper and Kropelin, 2006). A notable example is the decline of ancient Egyptian civilization around 4,000 years ago, which was believed to have been influenced in part by gradual drought in parts of the Sahara (Butzer, 2012). Understanding the mechanisms underlying such climatic transitions is therefore fundamental not only for paleoclimate research but also for interpreting the environmental context of human evolution and cultural development.

It is commonly known that orbital forcings, particularly precession-driven changes in seasonal insolation, are the dominant framework for explaining the occurrence of AHP. By modulating the interhemispheric summer insolation difference, orbital forcing influences the latitudinal position of the Intertropical Convergence Zone (ITCZ), thereby altering the intensity of the West African summer monsoon and regional precipitation patterns (Kutzbach, 1981; Pokras and Mix, 1987; DeMenocal, 2001). More broadly, many studies have frequently taken orbital parameters as the main explanatory clue to interpret geological records, including but not limited to monsoon systems worldwide (Cruz Jr et al., 2005; Cheng et al., 2016; Wen et al., 2024). Moreover, some theoretical and modeling studies have highlighted the critical roles of ice sheets and greenhouse gases, which introduce additional feedback through radiative forcing (Stouffer et al., 1989; Shi et al., 2025) and surface albedo changes (Manabe and Broccoli, 1985). These processes can substantially modulate the climatic response to orbital forcing. Therefore, discussions of the mechanisms underlying AHP should consider the combined influence of orbital forcing and non-orbital feedback.

Reconstructing the long-term climatic history of the Sahara is heavily based on geological archives, including marine sediments, lacustrine deposits, and terrestrial records (Demenocal et al., 2000; Sha et al., 2019; Cheddadi et al., 2021). However, many geological archives in North Africa remain incomplete because earlier deposits are frequently eroded and removed during high sea-level episodes, resulting in systematic gaps in the geological archive. Moreover, many reconstructions depend strongly on astronomical tuning to establish chronologies, which may introduce uncertainties and circular reasoning when orbital parameters are simultaneously invoked as explanatory mechanisms. This limitation is particularly critical for periods beyond the late Quaternary, where continuous and independently dated records are scarce. In this context, physically based numerical models provide an essential complementary approach by offering continuous, internally consistent reconstructions of climate variability, independent of geological archives. Recent modeling efforts have significantly advanced our understanding of Saharan climate dynamics by incorporating multiple forcings, including orbital parameters, ice sheets, and greenhouse gases (Armstrong et al., 2023; Duque-Villegas et al., 2022, 2025). These studies have demonstrated the importance of coupled forcings in shaping North African hydroclimate, yet most simulations have focused on relatively short intervals, such as the Holocene (Bian and Räisänen, 2024) or the Last glacial cycle (Li et al., 2022; Duque-Villegas et al., 2025), due to the high computational cost. As a result, the systematic quantification of individual forcing contributions over multi-million-year timescales remains limited.

Here, we address these challenges by conducting a series of targeted sensitivity experiments in which individual forcings are varied independently. This experimental design allows us to isolate and quantify the respective roles of orbital forcing,

https://doi.org/10.5194/egusphere-2026-5495
Preprint. Discussion started: 29 September 2026
© Author(s) 2026. CC BY 4.0 License.

ice sheets, and atmospheric CO_2 in controlling Saharan precipitation. Based on these experiments, we develop a physically constrained empirical framework that links external forcings to key intermediate climatic variables, Saharan precipitation, and vegetation fraction, and use it to reconstruct AHP variability continuously over the past 2.5 Ma. Compared to previous studies (Duque-Villegas et al., 2025; Armstrong et al., 2023; Duque-Villegas et al., 2022), our approach extends the temporal coverage of Saharan climate reconstructions while substantially reducing computational demands. The resulting precipitation time series provides insights into the mechanisms governing Green Sahara dynamics and a chronological reference that can support the interpretation and dating of fragmented geological and archaeological records across North Africa.

2 Data and Methods

2.1 Model simulations

The AWI Earth System Model (AWI-ESM) is used to evaluate the effects of individual forcings on AHP formation. The AWI-ESM is a coupled climate model consisting of the ocean and sea ice component FESOM and the atmospheric component ECHAM6, together with its land component JSBACH (Sidorenko et al., 2015, 2019). The performance of JSBACH in simulating vegetation has been evaluated against satellite- and observation-based datasets, showing skill in reproducing broad-scale vegetation cover and vegetation-related variables, despite remaining regional biases (Brovkin et al., 2013; Schneck et al., 2022). In our simulations, ECHAM6 employs a T63 Gaussian grid for the atmosphere, with a horizontal resolution of $1.875° \times 1.875°$ and 47 vertical levels. The ocean and sea ice component FESOM employs an unstructured mesh with spatially varying resolution, featuring relatively finer resolution in the polar regions, coastal areas, and along the equator, with grid spacing reaching up to approximately 25 km (Shi and Lohmann, 2016).

Previous studies have identified orbital forcing, particularly changes in Northern Hemisphere summer insolation associated with precession and obliquity, together with ice-sheet extent and atmospheric CO_2, as important controls on Saharan climate (Kutzbach, 1981; Claussen et al., 2017; Duque-Villegas et al., 2022). Accordingly, a total of 30 sensitivity experiments were performed, grouped into five categories (P360, C180, Imax, Omax, Omin), with each category containing multiple experimental realizations. Twenty-four time-slice simulations with different precession phases (0°, 15°, 30°, ..., 345°) were included in P360. Compared to P360, the CO_2 concentration in C180 was decreased to 180 ppmv, the same goes for Imax and included an added Northern Hemisphere ice sheet, equivalent to the condition in the Last Glacial Maximum (Argus et al., 2014). To maximize the impact of precession, the eccentricity and obliquity in P360, C180 and Imax experiments were set to 0.058 and 24.5° respectively. To ensure that the coupled system reached quasi-equilibrium conditions, each sensitivity experiment was integrated for 400 years in P360 and for at least 1,000 years in other categories. The climatological analyses presented in this study are based on the final 100 years of each simulation. Detailed parameters for each experiment are listed in Table 1. By comparing paired experiments, we can quantify the individual climate forcing in contributing AHP and build a simple model to reconstruct AHP during the long-term past.

https://doi.org/10.5194/egusphere-2026-5495
Preprint. Discussion started: 29 September 2026
© Author(s) 2026. CC BY 4.0 License.

Table 1. Parameter settings for each experiment.

Name	$c(CO_2)$ (ppmv)	Ice sheet	Eccentricity	Obliquity	Precession phase	Spin-up time
P360	284.32	Modern	0.058	24.5°	0°, 15°, . . . , 345°	300 years
C180	180	Modern	0.058	24.5°	90°, 270°	≥ 900 years
Imax	180	Large	0.058	24.5°	90°, 270°	≥ 900 years
Omin	284.32	Modern	0.016724	22°	270°	≥ 900 years
Omax	284.32	Modern	0.016724	24.5°	270°	≥ 900 years

2.2 Data for reconstructing AHP

Using the sensitivity experiments described above, we quantified the effects of precession, obliquity, ice-sheet extent, and atmospheric CO_2 on AHP formation. We then combined these calibrated relationships with time series of orbital parameters, atmospheric CO_2, and eustatic sea level to develop an empirical model for reconstructing AHP occurrence (see Sect. 4). The orbital parameters, including eccentricity, obliquity, and precession, were calculated following Laskar et al. (2004). For the past 800 ka, atmospheric CO_2 concentrations were obtained from Antarctic ice-core records (Lüthi et al., 2008; Bereiter et al., 2015), whereas eustatic sea level was taken from Bintanja et al. (2005). For the full 2.5-Ma reconstruction, both atmospheric CO_2 and sea level were obtained from the inverse forward modeling of Berends et al. (2021).

To validate our empirical model, we compare our results with existing reconstructions derived from climate-model simulations and geological records. The first model-based dataset comprises Saharan annual precipitation averaged over 15–30°N and 15°W–35°E (Armstrong et al., 2023). Using the paleo-conditioned coupled model HadCM3BB-v1.0, with atmospheric and oceanic horizontal grid spacings of $2.5° \times 3.75°$ and $1.25° \times 1.25°$, respectively, Armstrong et al. (2023) performed 219 snapshot simulations covering the past 800 ka. The simulated climatologies were subsequently interpolated to produce a continuous time series at 100-year intervals. The second dataset comprises pattern-scaled estimates of northern African vegetation change developed by Duque-Villegas et al. (2025). They conducted a 134-ka transient simulation to identify the dominant spatial mode of vegetation variability using MPI-ESM1.2 in its T31GR30 configuration. The atmospheric component ECHAM6.3 used a T31 grid (approximately $3.75° \times 3.75°$) with 31 vertical levels, whereas the ocean component MPIOM1.6 used the curvilinear GR30 grid, with a nominal horizontal resolution of approximately 3° and 40 vertical levels. Its temporal amplitude was then related to orbital forcing, greenhouse-gas radiative forcing, and Northern Hemisphere ice-sheet volume, allowing vegetation changes to be estimated over the past 800 ka. For comparison with our reconstruction, we use the resulting area-mean change in northern African vegetation fraction relative to pre-industrial conditions.

The geological records comprise marine sediment archives from the eastern Mediterranean and eastern tropical North Atlantic, together with speleothem records from the Levant. At ODP Site 967 in the eastern Mediterranean, the wet–dry index combines an X-ray fluorescence-derived principal component representing sapropel-associated monsoon runoff with an aeolian-dust record (Grant et al., 2017). The index captures the combined responses of runoff and dust deposition to North

https://doi.org/10.5194/egusphere-2026-5495
Preprint. Discussion started: 29 September 2026
© Author(s) 2026. CC BY 4.0 License.

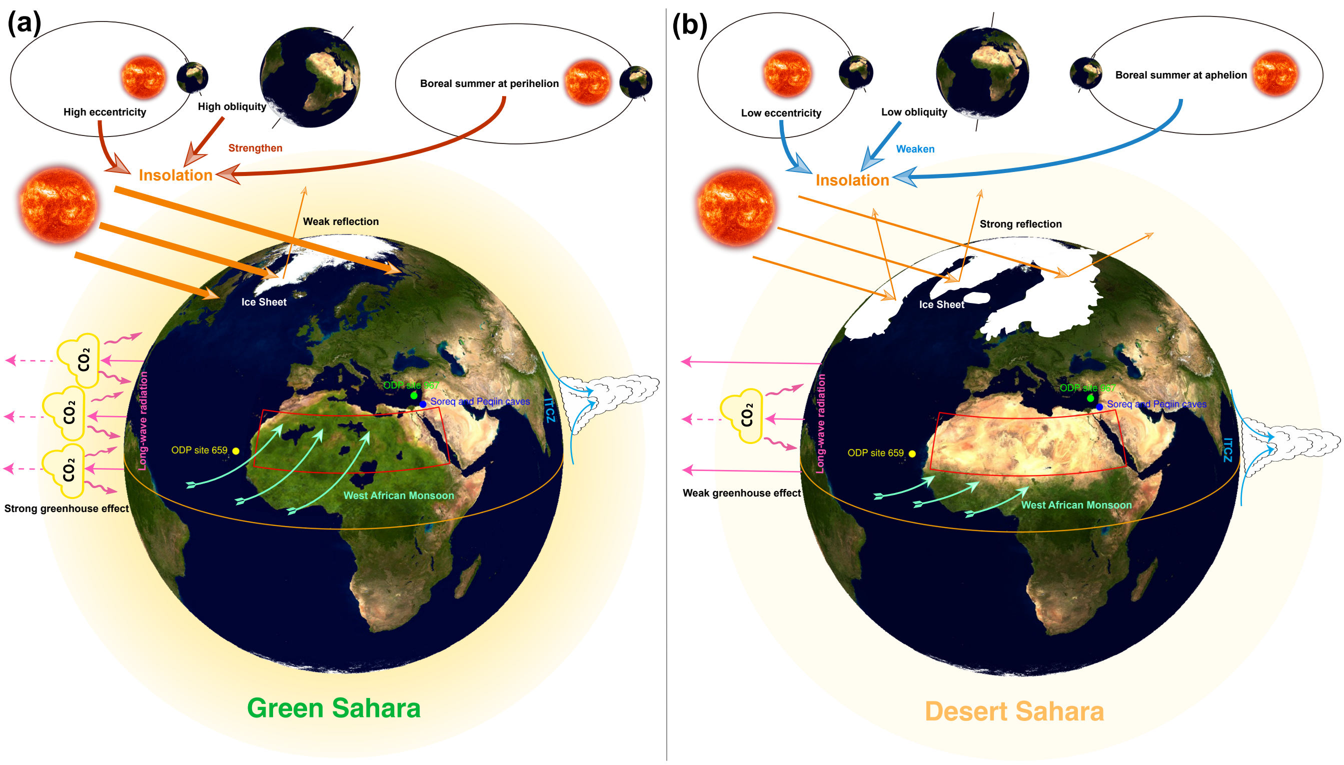

Figure 1. Study region (red rectangle), paleoclimate proxy sites, and conceptual mechanisms linking orbital forcing, ice-sheet extent, and atmospheric CO_2 to Green Sahara–desert transitions. Base-map imagery is derived from NASA Earth Observatory (https://science.nasa.gov/earth/earth-observatory/the-blue-marble-true-color-global-imagery-at-1km-resolution/).

African hydroclimatic variability. At ODP Site 659 in the eastern tropical North Atlantic, the $(\mathrm{Al}+\mathrm{Fe})/(\mathrm{Si}+\mathrm{K}+\mathrm{Ti})$ ratio records changes in the relative contributions of aeolian and riverine terrigenous material (Crocker et al., 2022). Saharan dust mobilization responds to aridity, surface moisture, vegetation cover, and wind strength, making this record an indicator of Saharan humid–arid transitions. For the interval since 127 ka, we additionally use speleothem calcite δ^{18}O records from the Soreq and Peqiin caves in the Levant (Bar-Matthews et al., 2003). These records reflect regional variations in rainfall, temperature, and the isotopic composition of eastern Mediterranean moisture, with lower δ^{18}O values during interglacial sapropel intervals indicating enhanced regional rainfall. Together, the speleothem records provide an additional regional comparison for hydroclimatic changes associated with strengthened North African monsoon runoff into the eastern Mediterranean. The locations of all geological archives are shown in Fig. 1.

https://doi.org/10.5194/egusphere-2026-5495
Preprint. Discussion started: 29 September 2026
© Author(s) 2026. CC BY 4.0 License.

2.3 Methods

2.3.1 Definition of latitude of ITCZ

Previous studies have proposed that the meridional migration of Intertropical Convergence Zone (ITCZ) contributes to the AHP (Wang et al., 2017; Bian and Räisänen, 2024). Here, we used the zonal-mean meridional position of ITCZ to quantify the amplitude of AHP. This position is defined as the latitude where the vertically averaged meridional stream function (700–300 hPa) crosses zero (Byrne et al., 2018). Regionally, the ITCZ position corresponds to the latitude of the maximum tropical precipitation (Kang et al., 2008).

2.3.2 Definition of AHP

Geological reconstructions of Saharan precipitation rely largely on vegetation indicators, including fossil pollen assemblages (Watrin et al., 2009; Cheddadi et al., 2021) and Saharan dust records (Grant et al., 2017; Crocker et al., 2022). Increased vegetation cover promotes pollen production and deposition while stabilizing the land surface and suppressing wind erosion and dust emissions (Ehrmann et al., 2017; Palchan and Torfstein, 2019). Consequently, these proxies primarily record precipitation-induced changes in vegetation and surface conditions rather than precipitation amount directly. To establish the precipitation–vegetation relationship, we extracted Saharan summer precipitation and the corresponding JSBACH-simulated vegetation fraction from the fully coupled AWI-ESM sensitivity experiments listed in Table 1. We then fitted a nonlinear relationship between regional mean maximum vegetation fraction and summer precipitation in the Sahara (Fig. 2). This relationship allows us to quantitatively compare vegetation-related proxies with reconstructed summer precipitation over the past 800 ka.

The vegetation threshold for defining AHP was calibrated using the timing of the most recent AHP, which has been broadly constrained to occur between approximately 5 and 15 ka BP (Demenocal et al., 2000), yielding a vegetation threshold of 19.9% which is close to the 80th percentile of the reconstructed vegetation value over the past 800 ka. To assess the influence of this threshold choice, we further performed a sensitivity analysis by varying the reference interval used for threshold calibration (Table S1). The results show that the reconstructed number of AHP remains relatively stable within the tested range, whereas the cumulative AHP time fraction is more sensitive to the threshold choice.

3 Dynamics for African Humid Period (AHP)

Using AWI-ESM (Sidorenko et al., 2015, 2019), we conducted a series of sensitivity experiments to investigate the dynamics of Saharan precipitation. By comparing paired experiments, we can quantify the contribution of each climate forcing to AHP (for detailed definitions, see Sect. 2).

While moisture supply from Northern Hemisphere mid-latitude westerlies contributes to rainfall in the northern Sahara (Cheddadi et al., 2021; Meyer et al., 2024), late-October precipitation associated with Tropical–Extratropical interactions, as well as winter storms, can also affect regional hydrology (Kuper and Kropelin, 2006; Dallmeyer et al., 2020). However, these

https://doi.org/10.5194/egusphere-2026-5495
Preprint. Discussion started: 29 September 2026
© Author(s) 2026. CC BY 4.0 License.

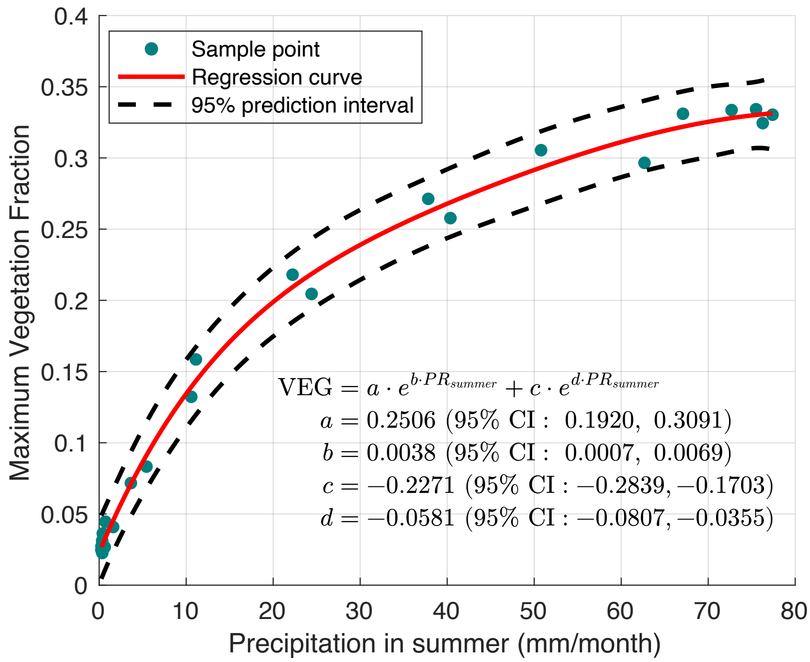

Figure 2. Relationship between Saharan summer precipitation and regional mean maximum vegetation fraction. Both variables were obtained from the fully coupled AWI-ESM sensitivity experiments listed in Table 1; vegetation fraction was simulated by the JSBACH land component. The red line shows the nonlinear fit, and the dashed lines show the 95% prediction interval.

events are spatially limited and episodic. Given that large-scale precipitation during AHP is dominated by boreal-summer monsoonal rainfall (Kutzbach, 1981; Claussen et al., 2017; Larrasoaña, 2021), our analysis focuses on this season, namely June, July, and August. The experiments reveal substantial precipitation changes linked to ITCZ shifts and West African summer monsoon strength (Fig. 3). Because the ITCZ position closely controls the summer monsoon (Geen et al., 2020), its southward displacement limits monsoon extent and suppresses Saharan rainfall. Furthermore, we find that a southward ITCZ displacement is associated with precession maximum, corresponding to perihelion in boreal winter, reduced obliquity, Northern Hemisphere ice-sheet expansion, and lower CO_2 levels (Fig. 3). The effect of CO_2 is comparatively minor due to its small prescribed variations.

Modern energetic theories provide a physical basis for interpreting these responses. Previous studies show that asymmetric hemispheric heating induces compensating cross-equatorial atmospheric energy transport. The zonal-mean ITCZ consequently tends to shift toward the more strongly heated hemisphere (Kang et al., 2008; Frierson and Hwang, 2012; Donohoe et al., 2013; Bischoff and Schneider, 2014; Schneider et al., 2014). Guided by this framework, we examined changes in vertically integrated atmospheric moist static energy (MSE) as a qualitative diagnostic of the atmospheric energy contrast between the hemispheres (Fig. 4). The increase in Earth-Sun distance reduces insolation in boreal summer when the precession phase changes from 90° to 270° (Fig. 4a); reduced CO_2 concentration leads to stronger cooling in the summer hemisphere (Fig. 4b); increased surface

https://doi.org/10.5194/egusphere-2026-5495
Preprint. Discussion started: 29 September 2026
© Author(s) 2026. CC BY 4.0 License.

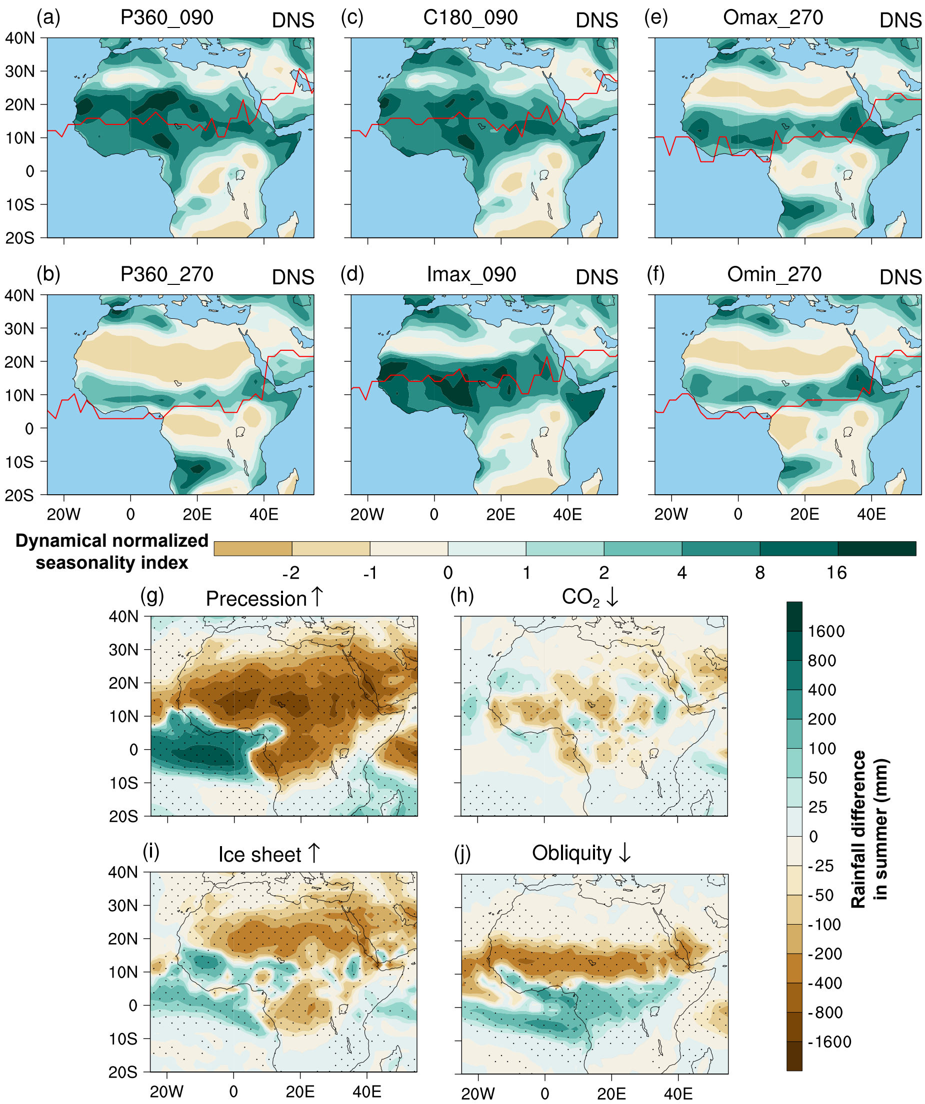

Figure 3. Southward ITCZ displacement is associated with a weaker Saharan summer monsoon and reduced precipitation. (a–f) Shading shows the monsoon index defined by Li and Zeng (2002). Area with values greater than 0 indicates monsoon regions. The meridional location of boreal summer ITCZ is marked by red line for each experiment; (g–j) The summer precipitation difference (shading) among different sensitivity experiments.

albedo enhances the reflection of solar radiation in the Northern Hemisphere (Fig. 4c); and reduced obliquity shifts the latitude of Earth's subsolar point southward during boreal summer (Fig. 4d). Collectively, these processes lead to a greater energy reduction in the Northern Hemisphere than in the Southern Hemisphere. Theoretically, a decrease in the interhemispheric energy difference will drive a southward ITCZ shift (Bischoff and Schneider, 2014; Schneider et al., 2014; Zhang et al., 2021) and thereby suppress Saharan summer precipitation.

https://doi.org/10.5194/egusphere-2026-5495
Preprint. Discussion started: 29 September 2026
© Author(s) 2026. CC BY 4.0 License.

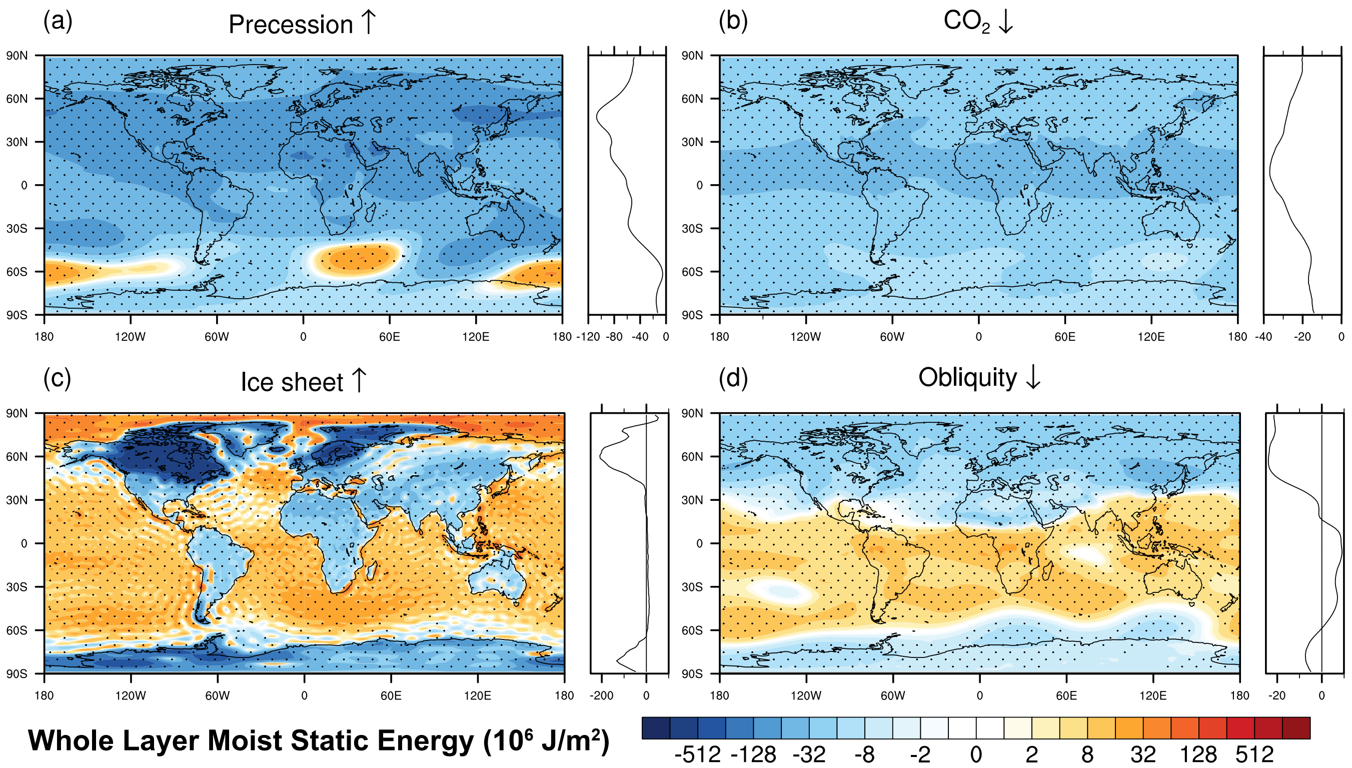

Figure 4. Differences of vertical integration of whole layer moist static energy (MSE) and its zonal average over all longitudes in summer caused by different factors. (a) When precession phase (longitude of perihelion) changes from 90°(the summer solstice at perihelion) to 270°(the summer solstice at aphelion) in P360; (b) When CO_2 concentration decreases (C180-P360); (c) When ice sheet extent increases (Imax-C180); (d) When obliquity decreases (Omin-Omax). The precession phase was set to 90°for (b)–(c) and 270°for (d). MSE h is the sum of sensible energy C_pT, latent energy Lq and geopotential energy gZ; the plotted whole-column quantity is $H = g^{-1}\int_{p_{\text{top}}}^{p_s} h\,\mathrm{d}p$.

Oceanic adjustment can further modulate this pathway (Zhao et al., 2005). We therefore analyzed SST differences to examine how the ocean participates in heat redistribution under different conditions. Forcing configurations unfavorable for AHP formation, as discussed in the MSE analysis, generally produce stronger cooling over the Northern Hemisphere oceans, especially over the North Atlantic (Fig. 5). Such SST changes can weaken the hemispheric thermal contrast and also lead to a southward displacement of the ITCZ.

Overall, our mechanism should be interpreted as a first-order energetic framework. External forcings modify the ITCZ latitude, and the resulting ITCZ displacement controls the West African summer monsoon and Saharan rainfall. At the same time, many complex feedback mechanisms within the climate system, such as ocean circulation (Pausata et al., 2017; Menviel et al., 2021), dust (Pausata et al., 2016; Zhou et al., 2023) and vegetation feedbacks (Lu et al., 2018; Berntell and Zhang, 2024), may also influence this process (Braconnot et al., 1999). However, we present only a few of the most direct and evident mechanisms in order to capture the most essential features behind it.

https://doi.org/10.5194/egusphere-2026-5495
Preprint. Discussion started: 29 September 2026
© Author(s) 2026. CC BY 4.0 License.

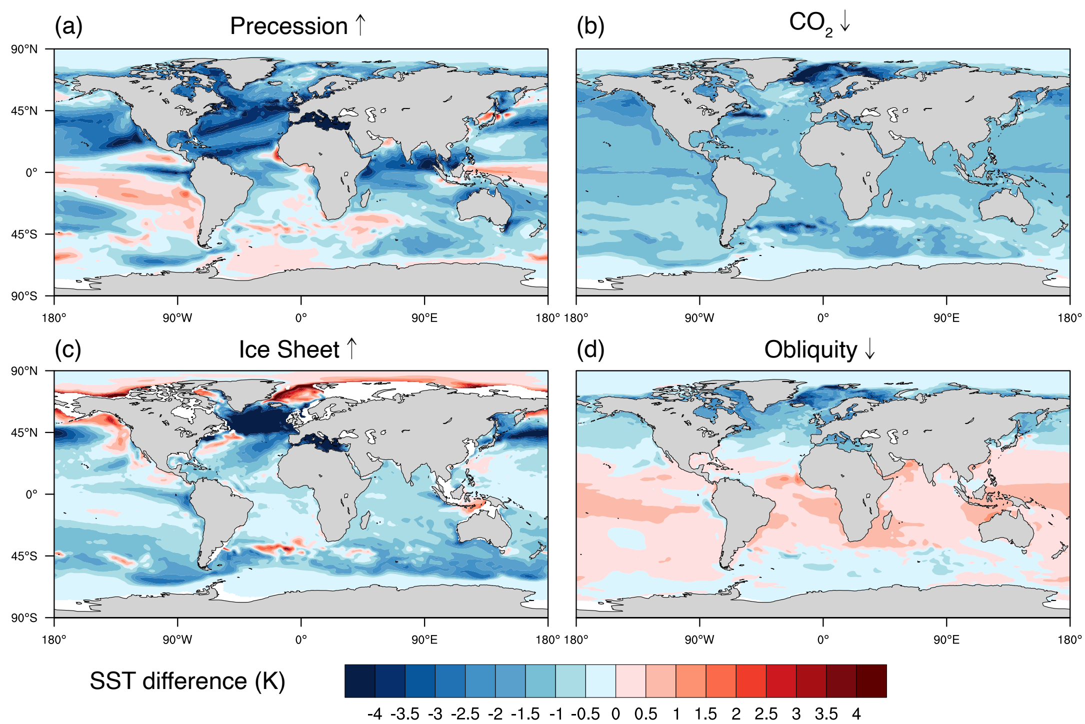

Figure 5. The summer SST difference among different sensitivity experiments. (a) When precession phase (longitude of perihelion) changes from 90°(the summer solstice at perihelion) to 270°(the summer solstice at aphelion) in P360; (b) When CO_2 concentration decreases (C180-P360); (c) When ice sheet extent increases (Imax-C180); (d) When obliquity decreases (Omin-Omax).

4 Development of a reconstruction framework

Building on the above logic, we quantified the combined effects of Earth's orbital parameters, CO_2 concentration and ice sheet extent on Saharan summer precipitation. Using the mean ITCZ latitude as a key metric, we developed a reduced-order framework based on three stages. First, it estimates the boreal-summer ITCZ latitude from predictors representing orbital configuration, ice-sheet extent, and atmospheric CO_2. Second, the estimated ITCZ latitude is mapped to Saharan summer precipitation using a separately fitted nonlinear relationship (Fig. 6b). Finally, precipitation is subsequently converted to vegetation fraction using the relationship shown in Fig. 2. The Earth's orbit is an ellipse with the equation:

$$\frac{x^2}{a^2} + \frac{y^2}{b^2} = 1 \quad (1)$$

where a is the semi-major axis, b is the semi-minor axis. The half of focal length c is equal to $\sqrt{a^2 - b^2}$. The Sun is located at the focal point $(-c, 0)$, and for any polar angle θ, the Earth's position is $(a\cos\theta, b\sin\theta)$. At the summer solstice, θ and the longitude of perihelion α will follow $\theta + \alpha = 3\pi/2$. Let d be the Sun-Earth distance, e be the eccentricity ($e = c/a$), then

© Author(s) 2026. CC BY 4.0 License.

$$d = \sqrt{(a\cos\theta + c)^2 + (b\sin\theta)^2} = a(1 - e\sin\alpha) \tag{2}$$

According to Wallace and Hobbs (2006), the total daily solar radiation Q can be expressed as

$$Q = \frac{T}{\pi}(\frac{a}{d})^2\overline{S_0}(\omega_0 \sin\varphi \sin\delta + \cos\varphi \cos\delta \sin\omega_0) \tag{3}$$

where T is one day's time, $\overline{S_0}$ is solar constant, δ is the declination, which is equal to obliquity at the summer solstice, φ is the latitude, and ω_0 is the solar hour angle when the sun rises, $\cos\omega_0 = -\tan\delta \cdot \tan\varphi$. Then, the total solar radiation in the Northern (Southern) hemisphere $Q_{NH(SH)}$ is

$$Q_{NH(SH)} = \iint Q dS_{NH(SH)} = \frac{T \cdot \overline{S_0}}{\pi(1 - e\sin\alpha)^2} \cdot \iint f(\varphi) dS_{NH(SH)} \tag{4}$$

The Surface integral $\iint f(\varphi)dS$ is equal to $\int_0^{2\pi} d\theta \int_{\varphi_1}^{\varphi_2} f(\varphi) R^2 \cos\varphi d\varphi$.

1. For the regions in the Arctic Circle, $\omega_0 = \pi$, $f(\varphi) = \pi \cdot \sin\varphi \cdot \sin\delta$, the integral upper and lower limits are $\pi/2$ and $\pi/2 - \delta$ respectively.

$$\iint f(\varphi)dS = \pi \sin\delta \int_0^{2\pi} d\theta \int_{\frac{\pi}{2}-\delta}^{\frac{\pi}{2}} \sin\varphi R^2 \cos\varphi d\varphi = \pi^2 R^2 \sin^3\delta \tag{5}$$

2. For the regions in the Antarctic Circle, $\omega_0 = 0$, $f(\varphi) = 0$, the integral is equal to 0.

3. For other regions, the integral upper and lower limits are $\pi/2 - \delta$ and 0 (0 and $\delta - \pi/2$) respectively for the Northern hemisphere NH (the Southern hemisphere SH).

$$\iint f(\varphi)dS = R^2 \int d\theta \int \left(\underbrace{\omega_0 \sin\varphi \cos\varphi \sin\delta}_{A} + \underbrace{\cos^2\varphi \cos\delta \sin\omega_0}_{B} \right) d\varphi \tag{6}$$

For part A in Eq. (6), the value of the difference between NH and SH is $\pi^2 R^2 \cos^2\delta \sin\delta$. Part B is an even function, so that the value of the difference between NH and SH is 0. When combining Eqs. (5) and (6) together, we can get the interhemispheric radiation flux difference Q_{NH-SH} as

$$\begin{aligned} Q_{NH-SH} &= \frac{T \cdot \overline{S_0}}{\pi(1 - e\sin\alpha)^2} \cdot (\iint f(\varphi) dS_{NH} - \iint f(\varphi) dS_{SH}) \\ &= \frac{T \cdot \overline{S_0}}{\pi(1 - e\sin\alpha)^2} \cdot (\pi^2 R^2 \cos^2\delta \sin\delta + \pi^2 R^2 \sin^3\delta) = k \cdot \frac{\sin\delta}{(1 - e\sin\alpha)^2} \end{aligned} \tag{7}$$

https://doi.org/10.5194/egusphere-2026-5495
Preprint. Discussion started: 29 September 2026
© Author(s) 2026. CC BY 4.0 License.

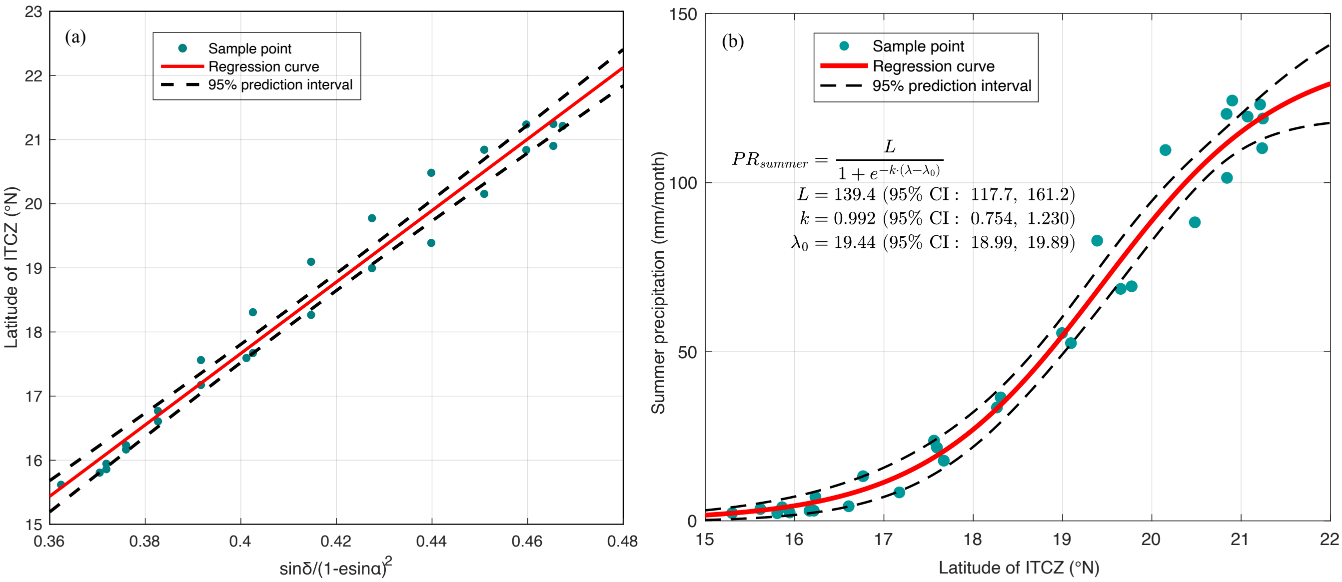

Figure 6. Calibration relationships used in the reduced-order reconstruction framework. (a) Linear relationship between the orbital radiation-contrast predictor and the simulated ITCZ latitude, based on the P360, Omin, and Omax experiments. (b) Logistic-sigmoid relationship between the simulated ITCZ latitude and Saharan summer precipitation across the sensitivity experiments. Teal circles represent individual simulations, red lines show the fitted regression curves, and black dashed lines indicate the 95% prediction intervals.

where k is a constant equal to $\pi T\overline{S_0}R^2$. This derivation provides an orbital-scale approximation of Q_{NH-SH}. Our sensitivity experiments show that there is an approximately linear relationship between Q_{NH-SH} and ITCZ latitude λ (Fig. 6a). Therefore, we use this physically motivated radiation contrast to represent the first-order orbital control on the summer ITCZ position. Let $x_1 = \sin\delta/(1-e\sin\alpha)^2$, then

$$\hat{\lambda} = k_1 x_1 + b_1 \tag{8}$$

Using P360, Omin and Omax for regression, we obtained k_1 and b_1.

The radiative influence of Northern Hemisphere ice sheets depends primarily on their surface area and on the incoming shortwave radiation available for reflection. To obtain a simple geometry-based proxy for ice-sheet area, we assume that the effective ice-sheet area S_{ice} scales with ice volume V_{NH} as

$$S_{\text{ice}} \propto V_{\text{NH}}^{2/3} \tag{9}$$

https://doi.org/10.5194/egusphere-2026-5495
Preprint. Discussion started: 29 September 2026
© Author(s) 2026. CC BY 4.0 License.

We use eustatic sea level rise (SLR) as an indicator of Northern Hemisphere ice volume. Following Moon et al. (2018), a sea-level rise of 7 m is used as a reference for the hypothetical complete loss of the Northern Hemispheric Ice Sheet. We therefore define the ice-sheet predictor as

$$x_2 = \begin{cases} (7 - \mathrm{SLR})^{2/3}, & \mathrm{SLR} < 7, \\ 0, & \mathrm{SLR} \geq 7. \end{cases} \tag{10}$$

This predictor provides a physically motivated measure of the potential ice-sheet influence on the summer energy budget. Because the albedo effect of ice sheets depends on incoming solar radiation, its climatic impact can vary with the orbital background state. We therefore represent the net ice-sheet contribution to the simulated ITCZ response using an empirical, dimensionless response factor,

$$M_{\mathrm{ice}}(x_2) = k_2 x_2 + b_2 \tag{11}$$

The orbital control derived above is then modulated by the ice-sheet response factor:

$$\hat{\lambda} = (k_1 x_1 + b_1) M_{\mathrm{ice}}(x_2) = (k_1 x_1 + b_1)(k_2 x_2 + b_2) \tag{12}$$

The coefficients k_2 and b_2 are constrained using the paired C180 and Imax simulations, which differ primarily in their prescribed ice-sheet boundary conditions.

According to Wigley (1987), the radiative forcing associated with a change in atmospheric CO_2 concentration can be approximated as

$$\Delta F_{\mathrm{CO_2}} = \alpha_{\mathrm{RF}} \ln\left(\frac{c}{c_0}\right) \tag{13}$$

where c and c_0 are the atmospheric CO_2 concentration in the perturbed and reference states, respectively, and α_{RF} is an effective radiative-forcing coefficient. This relationship motivates the use of a logarithmic CO_2 predictor. Changes in atmospheric CO_2 influence the ITCZ through coupled, state-dependent adjustments in atmospheric and oceanic circulation, temperature, clouds, water vapor, and surface feedbacks. A multiplicative form is used to represent state-dependent interactions, because CO_2 radiative forcing also depends on the background climate state (He et al., 2023). We therefore represent the net CO_2 contribution to the simulated ITCZ response using an empirical, dimensionless response factor diagnosed from the AWI-ESM sensitivity experiments:

$$M_{\mathrm{CO_2}}(x_3) = k_3 x_3 + b_3, \qquad x_3 = \ln c \tag{14}$$

The full reduced-order framework is consequently written as

$$\hat{\lambda} = (k_1 x_1 + b_1) M_{\mathrm{ice}}(x_2) M_{\mathrm{CO_2}}(x_3) = (k_1 x_1 + b_1)(k_2 x_2 + b_2)(k_3 x_3 + b_3) \tag{15}$$

https://doi.org/10.5194/egusphere-2026-5495
Preprint. Discussion started: 29 September 2026
© Author(s) 2026. CC BY 4.0 License.

where $x_1 = \sin\delta/(1-e\sin\alpha)^2$ represents the orbital configuration, $x_2 = [\max(7-\mathrm{SLR},0)]^{2/3}$ represents ice-sheet extent, and $x_3 = \ln c$ represents atmospheric CO_2 concentration. Here c is expressed numerically in ppmv, and SLR is expressed in metres relative to present-day sea level. The first factor gives the orbital baseline ITCZ latitude; the second and third are dimensionless modifiers. Thus, the three factors are not three separate ITCZ latitudes. The multiplicative form is an empirical representation of state-dependent interactions among the forcings, rather than a direct mathematical consequence of the insolation or radiative-forcing equations. The coefficients k_3 and b_3 are constrained using the paired P360 and C180 simulations. The fitted coefficients are provided in Table S2.

Based on all sensitivity experiments, we obtained a nonlinear regression between λ and the Saharan summer precipitation (15–30°N, 15°W–40°E) PR_{summer} (Fig. 6b).

$$PR_{\mathrm{summer}}(\hat{\lambda}) = \frac{L}{1+e^{-k\cdot(\hat{\lambda}-\lambda_0)}} \tag{16}$$

Then, PR_{summer} is converted to vegetation fraction VEG using the following fitted relationship (also shown in Fig. 2):

$$VEG(PR_{\mathrm{summer}}) = a\cdot e^{b\cdot PR_{\mathrm{summer}}} + c\cdot e^{d\cdot PR_{\mathrm{summer}}} \tag{17}$$

5 Validation of our reconstruction framework

To validate the performance of our semi-empirical framework, we reconstructed the Saharan climatic history over the past 800 ka (Fig. 7h) using atmospheric CO_2, ice sheet size (eustatic sea level), and Earth's orbital parameters. Although the framework first reconstructs Saharan summer precipitation, we define AHP using vegetation fraction. This is because many geological proxies, especially marine sediment records (Fig. 7e–f) are more closely related to vegetation rather than precipitation. In contrast, speleothem $\delta^{18}O$ records (Fig. 7g) constrain hydroclimate more broadly.

The reconstruction indicates that the AHP have emerged 24 times within the past 38 precession cycles during the past 800 ka, which means that not every precession cycle results in an AHP. This phenomenon could be also found in some geological records (Fig. 7e–g).

Comparison with paleoclimate archives shows that almost all of our reconstructed AHP appear in geologic records and the precession cycles without AHP are also largely reflected in geological records (Fig. 7). However, some proxy-indicated wet intervals, such as the peaks between AHP 13 and 14, are not identified as AHP in our reconstruction. Conversely, some reconstructed AHP, such as AHP 22, do not correspond to pronounced peaks in individual proxy records. In terms of time, the reconstructed AHP intervals do not always coincide exactly with the peaks in individual proxy records, and the peaks in the ODP 967 and ODP 659 records are themselves not always synchronous. These offsets may reflect differences in proxy sensitivity, source region, depositional environment, temporal resolution, and age-model uncertainty (Evans et al., 2013; Franke and Donner, 2019). In particular, the chronologies of the ODP 967 and ODP 659 marine sediment records are partly based on astronomical tuning (Grant et al., 2017; Crocker et al., 2022). Ages between chronological tie points in marine sediment records are commonly estimated by interpolation, which can introduce additional timing uncertainty when sedimentation rates vary

https://doi.org/10.5194/egusphere-2026-5495
Preprint. Discussion started: 29 September 2026
© Author(s) 2026. CC BY 4.0 License.

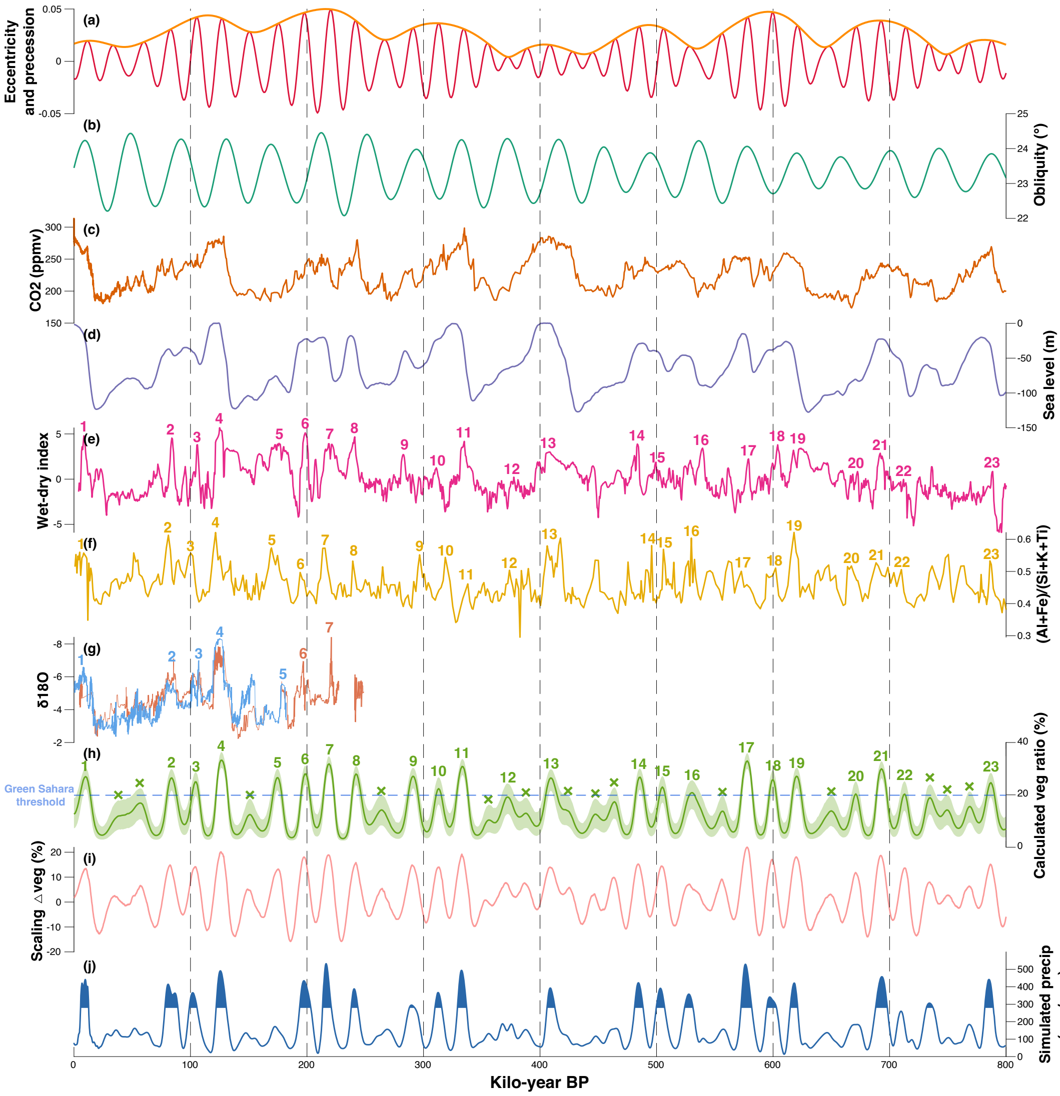

Figure 7. Control factors of Saharan humid conditions from proxy reconstructions and numerical simulations over the past 800 ka. (a–b) Eccentricity (orange), precession (red), and obliquity (cyan) calculated according to Laskar et al. (2004); (c) atmospheric carbon dioxide concentration from Lüthi et al. (2008); Bereiter et al. (2015); (d) eustatic sea-level reconstruction from Bintanja et al. (2005); (e) wet–dry index reconstructed from Ocean Drilling Program (ODP) site 967 (34.07°N, 32.72°E) (Grant et al., 2017); (f) (Al+Fe)/(Si+K+Ti) ratio from ODP site 659 (18.08°N, 21.03°W) (Crocker et al., 2022); (g) speleothem δ^{18}O records from Soreq Cave (blue) and Peqiin Cave (red) (Bar-Matthews et al., 2003); (h) calculated Saharan vegetation fraction and its 95% confidence interval (%, 15–30°N, 15°W–40°E), with the AHP threshold shown by the blue dotted line. Reconstructed AHP intervals are numbered, with the numbers also superimposed on the proxy records for visual comparison; crosses mark precession cycles in which no AHP is reconstructed. (i) Scaling vegetation ratio reconstructed using a pattern-scaling method (adapted from Fig. 6f of Duque-Villegas et al. (2025), distributed under the Creative Commons Attribution 4.0 License); (j) simulated Saharan annual precipitation (15–30°N, 15°W–35°E) from Armstrong et al. (2023).

https://doi.org/10.5194/egusphere-2026-5495
Preprint. Discussion started: 29 September 2026
© Author(s) 2026. CC BY 4.0 License.

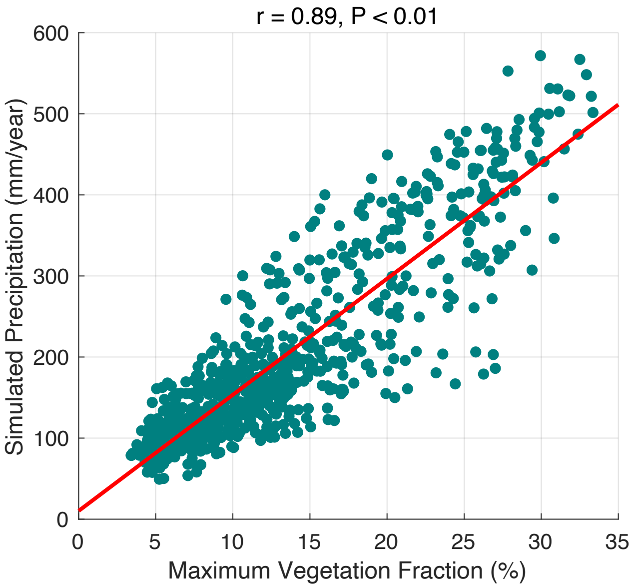

Figure 8. Comparison between the maximum vegetation fraction reconstructed by the reduced-order framework and the simulated Saharan precipitation (left) (Armstrong et al., 2023) and scaling vegetation ratio (Duque-Villegas et al., 2025).

(Franke and Donner, 2019; Peeters et al., 2023). In the last $\sim$ 100 ka, the reconstructed intensity of AHP shows good agreement with the paleoclimate archives, suggesting that both the timing and magnitude of humid phases are reasonably constrained. Further back in time, although the occurrence of AHP remains consistently captured by geological records, discrepancies in reconstructed intensity become more pronounced. This may be due to the declining capacity of geological archives to preserve quantitative information on precipitation intensity over long timescales (Franke and Donner, 2019). In addition, part of the discrepancy between our reconstruction and geological records may arise from the absence of internally driven abrupt climate events, such as Heinrich and Dansgaard–Oeschger events (Liu et al., 2001), which can substantially modulate hydroclimate conditions on millennial timescales but are not considered in our framework. Furthermore, the framework's simplified representation of regional precipitation dynamics (e.g., focusing solely on summer monsoon) could also contribute to the observed discrepancies.

Furthermore, to validate how well our derived curve aligns with the findings of previous studies, we compared our reconstruction with existing long transient simulations (Armstrong et al., 2023) and model-derived scaling vegetation (Duque-Villegas et al., 2025) in each time step over the past 800 ka, yielding strong correlation (R=0.89 and 0.93, respectively, Fig. 8). Importantly, unlike previous linear or empirical approximations, our reduced-order reconstruction framework is inherently nonlinear and enables interactions among multiple forcings to be represented more faithfully. Taken together, the consistency of our reconstruction with both geological evidence and numerical simulations gives us confidence to reasonably extend our framework, which would offer a computationally efficient yet robust tool for investigating long-term Saharan climate dynamics.

https://doi.org/10.5194/egusphere-2026-5495
Preprint. Discussion started: 29 September 2026
© Author(s) 2026. CC BY 4.0 License.

Table 2. Quantitative summary of reconstructed AHP occurrence across different Quaternary intervals and under extreme scenarios of atmospheric CO_2 and ice-sheet extent.

	Interval/scenario	Number of AHP	AHP per precession cycle	AHP time fraction
Basic reconstruction	0–0.82 Ma	24	63.2%	21.2%
	0.82–1.66 Ma	35	85.4%	29.6%
	1.66–2.5 Ma	30	73.2%	30.8%
	Total	89	74.2%	27.2%
Sensitivity scenarios	CO_2 maximum	90	75.0%	30.0%
	CO_2 minimum	85	70.8%	24.9%
	Ice sheet maximum	52	43.3%	10.8%
	Ice sheet minimum	104	86.7%	44.4%

However, this validation should be interpreted as evidence for the consistency and predictive performance of the reconstruction, rather than as definitive proof that the framework captures the complete underlying dynamical mechanism.

6 Reconstructing AHP across the Quaternary

Considering that our validation reveals an optimum capability in capturing the AHP in the past 800 ka, this give us confidence to extend the reconstruction of Saharan precipitation into the entire Quaternary (Fig. 9). Over the past 2.5 million years (Ma), AHP recurred on average every 28 ka, with many precession minima failing to produce wet conditions (Fig. 9j). An exception occurred during 0.82–1.66 Ma (green shading), when approximately 85% of the precession cycles were associated with AHP formation (Table 2). This is because the eccentricity rarely remained in a prolonged low-value state (Fig. 9a). In contrast, prolonged intervals of low eccentricity during other periods coincided with more frequent absence of AHP (blue shading, Fig. 9). In addition, compared with the past 0.8 Ma, this interval (0.82-1.66 Ma) was characterized by relatively smaller ice sheets and higher atmospheric CO_2 (Fig. 9c–d), which likely favored more frequent greening events.

We further explored the possible modifying effects of atmospheric CO_2 and ice sheet on reconstructed Saharan climate (Table 2). Higher atmospheric CO_2 concentration tends to increase the number of AHP and extend their duration. The effects of ice sheet appear to be stronger: under conditions of minimal ice sheet area, AHP appear in almost every precession cycle, and nearly half of the entire Quaternary is occupied by AHP. It is important to note that our analysis isolates the individual effects of ice sheets and CO_2. Although the direct impact of CO_2 on Saharan climate appears comparatively modest, CO_2 is widely recognized as a major control on global ice volume through its radiative forcing and feedback in the climate system (Berends et al., 2021; Hain and Sigman, 2024). Therefore, its indirect impact on Saharan climate cannot be ignored. It is worth

https://doi.org/10.5194/egusphere-2026-5495
Preprint. Discussion started: 29 September 2026
© Author(s) 2026. CC BY 4.0 License.

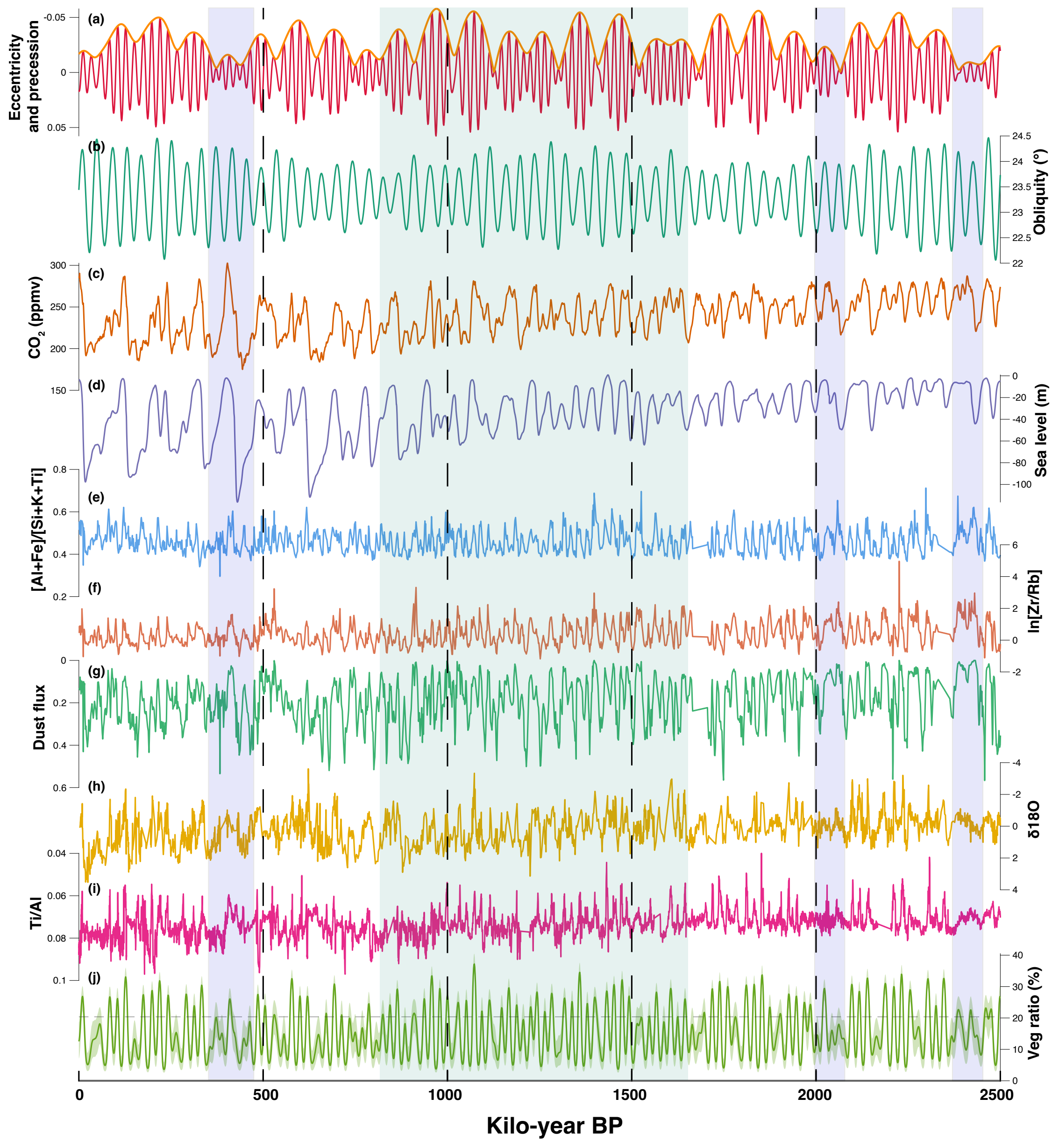

Figure 9. Reconstruction of AHP and their control factors across the Quaternary. (a–b) Eccentricity (orange), precession (red) and obliquity (cyan) calculated following Laskar et al. (2004); (c–d) Atmospheric CO_2 concentration and sea level reconstructions from Berends et al. (2021); (e–g) (Al+Fe)/(Si+K+Ti) (blue), ln (Zr/Rb) XRF core scan ratios (brown) and estimated dust flux (green) from ODP site 659 (18.08°N, 21.03°W) (Crocker et al., 2022); (h–i) $\delta^{18}O$ (yellow) and Ti/Al ratio (pink) from ODP site 967 (34.07°N, 32.72°E) (Grant et al., 2022); (j) Reconstructed Saharan vegetation fraction and its 95% confidence intervals (%, 15–30°N, 15°W–40°E). The green shading highlights the 0.82–1.66 Ma interval, and the blue shading marks representative intervals of persistently low eccentricity.

noting that such statistics are partially influenced by the adopted AHP threshold (Table S1) and should therefore be interpreted with caution.

To our knowledge, this study represents the first attempt to extend a reconstruction framework explicitly constrained by numerical simulations to the entire Quaternary, providing a complementary perspective for evaluating existing geological records. The chronology of many geological records relies on astronomical tuning (Lisiecki and Raymo, 2005), in which the rhythm of AHP is aligned with Northern Hemisphere summer insolation. However, our study corroborates earlier results that non-orbital boundary conditions, such as ice sheets, also make important contributions to AHP (Claussen et al., 2017). Considering the contributions of these factors will help improve the accuracy of reconstructing the timing and intensity of AHP, particularly for early Quaternary records (Fig. 7e–j).

7 Discussion and conclusions

Using targeted AWI-ESM sensitivity experiments, we developed an empirical framework to reconstruct Quaternary Saharan climate from orbital parameters, eustatic sea level, and atmospheric CO_2. The experiments indicate that these three factors influence the West African summer monsoon and Saharan rainfall by altering the position of the Intertropical Convergence Zone (ITCZ). Orbital forcing determines when humid conditions may occur, whereas ice sheets and CO_2 modulate whether favorable orbital conditions shift the ITCZ sufficiently northward to produce a humid Sahara. The framework uses these relationships to estimate ITCZ latitude and, subsequently, Saharan precipitation and vegetation cover. We evaluated the framework against geological records and numerical simulations covering the past 800 ka, showing optimum results (Fig. 7). And the reconstructed vegetation fraction is strongly correlated with existing numerical simulations (Fig. 8) (Armstrong et al., 2023; Duque-Villegas et al., 2025). We then applied the framework to reconstruct Saharan climate throughout the Quaternary.

The main practical advantage of this framework is that 30 climate-model experiments were used to understand the dynamics of AHP, which enable us to build up an empirical model to calculate a continuous 2.5-Ma record without simulating every time slice. This design substantially reduces the computational cost of reconstructing long climate sequences. The framework can therefore identify periods that warrant more detailed simulations or proxy sampling, allowing computational and observational resources to be concentrated on key intervals. It may also provide additional constraints for chronological analysis. Astronomical tuning commonly aligns humid intervals with changes in Northern Hemisphere summer insolation (Lisiecki and Raymo, 2005). Our reconstruction, however, indicates that some apparently favorable precession cycles may be suppressed by large ice sheets or low CO_2. The reconstructed AHP windows can therefore be combined with radiometric ages and stratigraphic relationships to compare alternative age models. It may also contribute to interdisciplinary studies, particularly in archaeology, which may help refine timelines of human expansion out of Africa (Kuper and Kropelin, 2006; Larrasoaña, 2021).

However, our empirical model inevitably has some limits. First, it represents only the first-order interactions among orbital forcing, ice sheets, and CO_2. Because the framework uses eustatic sea level as a proxy for ice-sheet extent, it does not distinguish ice-sheet effects from the direct climatic influence of sea-level change. Changes in terrestrial elevation and ocean

© Author(s) 2026. CC BY 4.0 License.

bathymetry associated with sea-level variation can themselves reorganize atmospheric and oceanic circulation (Zhang et al., 2023). Moreover, it does not resolve all lags, thresholds, or hysteretic responses, and it considers only mean Saharan summer rainfall. The framework also simplifies or omits millennial-scale climate variability and several nonlinear feedbacks. These include aerosols (Dong and Sutton, 2015), dynamic vegetation (Menviel et al., 2021; Lu et al., 2018; Berntell and Zhang, 2024), dust (Pausata et al., 2016; Zhou et al., 2023), and ocean circulation (Pausata et al., 2017; Menviel et al., 2021; Zhao et al., 2005). These processes could either amplify or weaken the monsoon response. Finally, the precipitation–vegetation relationship is calibrated using JSBACH alone and may vary among vegetation models (Hopcroft et al., 2017).

Future work should broaden the calibration and validation of the empirical model. Fully coupled simulations should span higher CO_2 concentrations, multiple orbital configurations, and a wider range of ice-sheet extents to test whether the fitted relationships remain valid outside the present calibration range. Combining results from several Earth system models would reduce the dependence of the empirical model on AWI-ESM alone. Overall, we developed a computationally efficient empirical model constrained by climate-model experiments for continuous reconstruction of Quaternary Saharan climate, although further validation is needed.

Code and data availability. Code will be available on request. All AWI-ESM simulation output data can be downloaded from https://zenodo.org/records/15846096.

Author contributions. Hu Yang designed the study and performed the AWI-ESM simulations. Hang Wang analyzed the data and contributed to the development of the theoretical model. Hang Wang and Hu Yang wrote the initial draft. All authors contributed to the discussion and revision of the manuscript.

Competing interests. The authors declare that they have no conflict of interest.

Acknowledgements. This study was jointly supported by the construction fund of the Frontier Research Center at the Southern Marine Science and Engineering Guangdong Laboratory (Zhuhai) (grant no. SML2023SP204), the National Natural Science Foundation of China (grant no. 42206256), and the Ocean Negative Carbon Emissions (ONCE) programme.

https://doi.org/10.5194/egusphere-2026-5495
Preprint. Discussion started: 29 September 2026
© Author(s) 2026. CC BY 4.0 License.

References

Argus, D. F., Peltier, W. R., Drummond, R., and Moore, A. W.: The Antarctica component of postglacial rebound model ICE-6G_C (VM5a) based on GPS positioning, exposure age dating of ice thicknesses, and relative sea level histories, Geophysical Journal International, 198, 537–563, https://doi.org/10.1093/gji/ggu140, 2014.

Armstrong, E., Tallavaara, M., Hopcroft, P. O., and Valdes, P. J.: North African humid periods over the past 800,000 years, Nature Communications, 14, 5549, https://doi.org/10.1038/s41467-023-41219-4, 2023.

Bar-Matthews, M., Ayalon, A., Gilmour, M., Matthews, A., and Hawkesworth, C. J.: Sea-land oxygen isotopic relationships from planktonic foraminifera and speleothems in the Eastern Mediterranean region and their implication for paleorainfall during interglacial intervals, Geochimica et cosmochimica acta, 67, 3181–3199, https://doi.org/10.1016/S0016-7037(02)01031-1, 2003.

Barth, H.: Travels and Discoveries in North and Central Africa: Being a Journal of an Expedition Undertaken Under the Auspices of H.B.M.'s Government, in the Years 1849–1855, vol. 1, Longman, Brown, Green, Longmans & Roberts, London, https://www.gutenberg.org/ebooks/76316, 1857.

Bereiter, B., Eggleston, S., Schmitt, J., Nehrbass-Ahles, C., Stocker, T. F., Fischer, H., Kipfstuhl, S., and Chappellaz, J.: Revision of the EPICA Dome C CO2 record from 800 to 600 kyr before present, Geophysical Research Letters, 42, 542–549, https://doi.org/10.1002/2014GL061957, 2015.

Berends, C. J., De Boer, B., and Van De Wal, R. S.: Reconstructing the evolution of ice sheets, sea level, and atmospheric CO2 during the past 3.6 million years, Climate of the Past, 17, 361–377, https://doi.org/10.5194/cp-17-361-2021, 2021.

Berntell, E. and Zhang, Q.: Mid-Holocene West African monsoon rainfall enhanced in EC-Earth simulation with dynamic vegetation feedback, Climate Dynamics, 62, 7001–7017, https://doi.org/10.1007/s00382-024-07262-7, 2024.

Bian, J. and Räisänen, J.: Mid-holocene changes in the global ITCZ: meridional structure and land-sea rainfall differences, Climate Dynamics, 62, 10 683–10 701, https://doi.org/10.1007/s00382-024-07470-1, 2024.

Bintanja, R., Van De Wal, R. S., and Oerlemans, J.: Modelled atmospheric temperatures and global sea levels over the past million years, Nature, 437, 125–128, https://doi.org/10.1038/nature03975, 2005.

Bischoff, T. and Schneider, T.: Energetic constraints on the position of the intertropical convergence zone, Journal of Climate, 27, 4937–4951, https://doi.org/10.1175/JCLI-D-13-00650.1, 2014.

Braconnot, P., Joussaume, S., Marti, O., and De Noblet, N.: Synergistic feedbacks from ocean and vegetation on the African monsoon response to mid-Holocene insolation, Geophysical Research Letters, 26, 2481–2484, https://doi.org/10.1029/1999GL006047, 1999.

Brovkin, V., Boysen, L., Raddatz, T., Gayler, V., Loew, A., and Claussen, M.: Evaluation of vegetation cover and land-surface albedo in MPI-ESM CMIP5 simulations, Journal of Advances in Modeling Earth Systems, 5, 48–57, https://doi.org/10.1029/2012MS000169, 2013.

Butzer, K. W.: Collapse, environment, and society, Proceedings of the national Academy of Sciences, 109, 3632–3639, https://doi.org/10.1073/pnas.1114845109, 2012.

Byrne, M. P., Pendergrass, A. G., Rapp, A. D., and Wodzicki, K. R.: Response of the intertropical convergence zone to climate change: Location, width, and strength, Current climate change reports, 4, 355–370, https://doi.org/10.1007/s40641-018-0110-5, 2018.

Cheddadi, R., Carré, M., Nourelbait, M., François, L., Rhoujjati, A., Manay, R., Ochoa, D., and Schefuß, E.: Early Holocene greening of the Sahara requires Mediterranean winter rainfall, Proceedings of the National Academy of Sciences, 118, e2024898 118, https://doi.org/10.1073/pnas.2024898118, 2021.

© Author(s) 2026. CC BY 4.0 License.

Cheng, H., Edwards, R. L., Sinha, A., Spötl, C., Yi, L., Chen, S., Kelly, M., Kathayat, G., Wang, X., Li, X., et al.: The Asian monsoon over the past 640,000 years and ice age terminations, nature, 534, 640–646, https://doi.org/10.1038/nature18591, 2016.

Claussen, M., Dallmeyer, A., and Bader, J.: Theory and modeling of the African humid period and the green Sahara, Oxford research encyclopedia of climate science, https://doi.org/10.1093/acrefore/9780190228620.013.532, 2017.

Crocker, A. J., Naafs, B. D. A., Westerhold, T., James, R. H., Cooper, M. J., Röhl, U., Pancost, R. D., Xuan, C., Osborne, C. P., Beerling, D. J., et al.: Astronomically controlled aridity in the Sahara since at least 11 million years ago, Nature Geoscience, 15, 671–676, https://doi.org/10.1038/s41561-022-00990-7, 2022.

Cruz Jr, F. W., Burns, S. J., Karmann, I., Sharp, W. D., Vuille, M., Cardoso, A. O., Ferrari, J. A., Silva Dias, P. L., and Viana Jr, O.: Insolation-driven changes in atmospheric circulation over the past 116,000 years in subtropical Brazil, Nature, 434, 63–66, https://doi.org/10.1038/nature03365, 2005.

Dallmeyer, A., Claussen, M., Lorenz, S. J., and Shanahan, T.: The end of the African humid period as seen by a transient comprehensive Earth system model simulation of the last 8000 years, Climate of the Past, 16, 117–140, https://doi.org/10.5194/cp-16-117-2020, 2020.

Demenocal, P., Ortiz, J., Guilderson, T., Adkins, J., Sarnthein, M., Baker, L., and Yarusinsky, M.: Abrupt onset and termination of the African Humid Period:: rapid climate responses to gradual insolation forcing, Quaternary science reviews, 19, 347–361, https://doi.org/10.1016/S0277-3791(99)00081-5, 2000.

DeMenocal, P. B.: Cultural responses to climate change during the late Holocene, Science, 292, 667–673, https://doi.org/10.1126/science.1059287, 2001.

Dong, B. and Sutton, R.: Dominant role of greenhouse-gas forcing in the recovery of Sahel rainfall, Nature Climate Change, 5, 757–760, https://doi.org/10.1038/nclimate2664, 2015.

Donohoe, A., Marshall, J., Ferreira, D., and McGee, D.: The relationship between ITCZ location and cross-equatorial atmospheric heat transport: From the seasonal cycle to the Last Glacial Maximum, Journal of Climate, 26, 3597–3618, https://doi.org/10.1175/JCLI-D-12-00467.1, 2013.

Duque-Villegas, M., Claussen, M., Brovkin, V., and Kleinen, T.: Effects of orbital forcing, greenhouse gases and ice sheets on Saharan greening in past and future multi-millennia, Climate of the Past, 18, 1897–1914, https://doi.org/10.5194/cp-18-1897-2022, 2022.

Duque-Villegas, M., Claussen, M., Kleinen, T., Bader, J., and Reick, C. H.: Pattern scaling of simulated vegetation change in northern Africa during glacial cycles, Climate of the Past, 21, 773–794, https://doi.org/10.5194/cp-21-773-2025, 2025.

Ehrmann, W., Schmiedl, G., Beuscher, S., and Krüger, S.: Intensity of African humid periods estimated from Saharan dust fluxes, PloS one, 12, e0170 989, https://doi.org/10.1371/journal.pone.0170989, 2017.

El-Shenawy, M. I., Kim, S.-T., Schwarcz, H. P., Asmerom, Y., and Polyak, V. J.: Speleothem evidence for the greening of the Sahara and its implications for the early human dispersal out of sub-Saharan Africa, Quaternary Science Reviews, 188, 67–76, https://doi.org/10.1016/j.quascirev.2018.03.016, 2018.

Evans, M. N., Tolwinski-Ward, S. E., Thompson, D. M., and Anchukaitis, K. J.: Applications of proxy system modeling in high resolution paleoclimatology, Quaternary Science Reviews, 76, 16–28, https://doi.org/10.1016/j.quascirev.2013.05.024, 2013.

Franke, J. G. and Donner, R. V.: Correlating paleoclimate time series: Sources of uncertainty and potential pitfalls, Quaternary science reviews, 212, 69–79, https://doi.org/10.1016/j.quascirev.2019.03.017, 2019.

Frierson, D. M. W. and Hwang, Y.-T.: Extratropical influence on ITCZ shifts in slab ocean simulations of global warming, Journal of Climate, 25, 720–733, https://doi.org/10.1175/JCLI-D-11-00116.1, 2012.

© Author(s) 2026. CC BY 4.0 License.

Geen, R., Bordoni, S., Battisti, D. S., and Hui, K.: Monsoons, ITCZs, and the concept of the global monsoon, Reviews of Geophysics, 58, e2020RG000 700, https://doi.org/10.1029/2020RG000700, 2020.

Grant, K. M., Rohling, E. J., Westerhold, T., Zabel, M., Heslop, D., Konijnendijk, T., and Lourens, L.: A 3 million year index for North African humidity/aridity and the implication of potential pan-African Humid periods, Quaternary Science Reviews, 171, 100–118, https://doi.org/10.1016/j.quascirev.2017.07.005, 2017.

Grant, K. M., Amarathunga, U., Amies, J. D., Hu, P., Qian, Y., Penny, T., Rodriguez-Sanz, L., Zhao, X., Heslop, D., Liebrand, D., et al.: Organic carbon burial in Mediterranean sapropels intensified during Green Sahara Periods since 3.2 Myr ago, Communications Earth & Environment, 3, 11, https://doi.org/10.1038/s43247-021-00339-9, 2022.

Hain, M. P. and Sigman, D. M.: CO2 in Earth's ice age cycles, Oxford Research Encyclopedia of Climate Science, https://doi.org/10.1093/acrefore/9780190228620.013.879, 2024.

He, H., Kramer, R. J., Soden, B. J., and Jeevanjee, N.: State dependence of CO2 forcing and its implications for climate sensitivity, Science, 382, 1051–1056, https://doi.org/10.1126/science.abq6872, 2023.

Hopcroft, P. O., Valdes, P. J., Harper, A. B., and Beerling, D. J.: Multi vegetation model evaluation of the Green Sahara climate regime, Geophysical Research Letters, 44, 6804–6813, https://doi.org/10.1002/2017GL073740, 2017.

Kang, S. M., Held, I. M., Frierson, D. M., and Zhao, M.: The response of the ITCZ to extratropical thermal forcing: Idealized slab-ocean experiments with a GCM, Journal of Climate, 21, 3521–3532, https://doi.org/10.1175/2007JCLI2146.1, 2008.

Kuper, R.: Wadi Howar and Laqiya: Recent Field Studies into the Early Settlement of the Northern Sudan, in: Nubische Studien: Tagungsakten der 5. Internationalen Konferenz der International Society for Nubian Studies, Heidelberg, 22.–25. September 1982, edited by Krause, M., pp. 129–136, P. von Zabern, Mainz am Rhein, ISBN 978-3-8053-0878-6, https://www.ifao.egnet.net/bases/beo/beo3806, 1986.

Kuper, R. and Kropelin, S.: Climate-controlled Holocene occupation in the Sahara: motor of Africa's evolution, science, 313, 803–807, https://doi.org/10.1126/science.1130989, 2006.

Kutzbach, J. E.: Monsoon climate of the early Holocene: climate experiment with the earth's orbital parameters for 9000 years ago, Science, 214, 59–61, https://doi.org/10.1126/science.214.4516.59, 1981.

Larrasoaña, J. C.: A review of West African monsoon penetration during Green Sahara periods; implications for human evolution and dispersals over the last three million years, Oxford Open Climate Change, 1, kgab011, https://doi.org/10.1093/oxfclm/kgab011, 2021.

Larrasoaña, J. C., Roberts, A. P., and Rohling, E. J.: Dynamics of green Sahara periods and their role in hominin evolution, PloS one, 8, e76 514, https://doi.org/10.1371/journal.pone.0076514, 2013.

Laskar, J., Robutel, P., Joutel, F., Gastineau, M., Correia, A. C., and Levrard, B.: A long-term numerical solution for the insolation quantities of the Earth, Astronomy & Astrophysics, 428, 261–285, https://doi.org/10.1051/0004-6361:20041335, 2004.

Li, H., Renssen, H., and Roche, D. M.: Comparison of the green-to-desert Sahara transitions between the Holocene and the last interglacial, Climate of the Past, 18, 2303–2319, https://doi.org/10.5194/cp-18-2303-2022, 2022.

Li, J. and Zeng, Q.: A unified monsoon index, Geophysical Research Letters, 29, 115–1–115–4, https://doi.org/10.1029/2001GL013874, 2002.

Lisiecki, L. E. and Raymo, M. E.: A Pliocene-Pleistocene stack of 57 globally distributed benthic δ18O records, Paleoceanography, 20, https://doi.org/10.1029/2004PA001071, 2005.

Liu, J., Ni, Y., and Chu, G.: Main palaeoclimatic events in the Quaternary, Quaternary Sciences, 21, 239–248, http://www.dsjyj.com.cn/article/id/dsjyj_9407, in Chinese, 2001.

https://doi.org/10.5194/egusphere-2026-5495
Preprint. Discussion started: 29 September 2026
© Author(s) 2026. CC BY 4.0 License.

Lu, Z., Miller, P. A., Zhang, Q., Zhang, Q., Wårlind, D., Nieradzik, L., Sjolte, J., and Smith, B.: Dynamic vegetation simulations of the mid-Holocene Green Sahara, Geophysical Research Letters, 45, 8294–8303, https://doi.org/10.1029/2018GL079195, 2018.

Lüthi, D., Le Floch, M., Bereiter, B., Blunier, T., Barnola, J.-M., Siegenthaler, U., Raynaud, D., Jouzel, J., Fischer, H., Kawamura, K., et al.: High-resolution carbon dioxide concentration record 650,000-800,000 years before present, nature, 453, 379–382, https://doi.org/10.1038/nature06949, 2008.

Manabe, S. and Broccoli, A.: The influence of continental ice sheets on the climate of an ice age, Journal of Geophysical Research: Atmospheres, 90, 2167–2190, https://doi.org/10.1029/JD090iD01p02167, 1985.

Menviel, L., Govin, A., Avenas, A., Meissner, K. J., Grant, K. M., and Tzedakis, P. C.: Drivers of the evolution and amplitude of African Humid Periods, Communications Earth & Environment, 2, 237, https://doi.org/10.1038/s43247-021-00309-1, 2021.

Meyer, V. D., Pätzold, J., Mollenhauer, G., Castañeda, I. S., Schouten, S., and Schefuß, E.: Evolution of winter precipitation in the Nile-River watershed since the last glacial, Climate of the Past, 20, 523–546, https://doi.org/10.5194/cp-20-523-2024, 2024.

Moon, T., Ahlstrøm, A., Goelzer, H., Lipscomb, W., and Nowicki, S.: Rising oceans guaranteed: Arctic land ice loss and sea level rise, Current climate change reports, 4, 211–222, https://doi.org/10.1007/s40641-018-0107-0, 2018.

Palchan, D. and Torfstein, A.: A drop in Sahara dust fluxes records the northern limits of the African Humid Period, Nature Communications, 10, 3803, https://doi.org/10.1038/s41467-019-11701-z, 2019.

Pausata, F. S., Messori, G., and Zhang, Q.: Impacts of dust reduction on the northward expansion of the African monsoon during the Green Sahara period, Earth and Planetary Science Letters, 434, 298–307, https://doi.org/10.1016/j.epsl.2015.11.049, 2016.

Pausata, F. S., Zhang, Q., Muschitiello, F., Lu, Z., Chafik, L., Niedermeyer, E. M., Stager, J. C., Cobb, K. M., and Liu, Z.: Greening of the Sahara suppressed ENSO activity during the mid-Holocene, Nature Communications, 8, 16 020, https://doi.org/10.1038/ncomms16020, 2017.

Peeters, F. J. C., van der Lubbe, H. J. L., and Scussolini, P.: Age-depth models for tropical marine hemipelagic deposits improve significantly when proxy-based information on sediment composition is included, Paleoceanography and Paleoclimatology, 38, e2022PA004 476, https://doi.org/10.1029/2022PA004476, 2023.

Pokras, E. M. and Mix, A. C.: Earth's precession cycle and Quaternary climatic change in tropical Africa, Nature, 326, 486–487, https://doi.org/10.1038/326486a0, 1987.

Schandelmeier, H. and Thorweihe, U.: Geoscientific research in northeast Africa, CRC Press, Boca Raton, https://doi.org/10.1201/9780203753392, 2017.

Schneck, R., Gayler, V., Nabel, J. E., Raddatz, T., Reick, C. H., and Schnur, R.: Assessment of JSBACHv4. 30 as a land component of ICON-ESM-V1 in comparison to its predecessor JSBACHv3. 2 of MPI-ESM1. 2, Geoscientific Model Development, 15, 8581–8611, https://doi.org/10.5194/gmd-15-8581-2022, 2022.

Schneider, T., Bischoff, T., and Haug, G. H.: Migrations and dynamics of the intertropical convergence zone, Nature, 513, 45–53, https://doi.org/10.1038/nature13636, 2014.

Sha, L., Ait Brahim, Y., Wassenburg, J. A., Yin, J., Peros, M., Cruz, F. W., Cai, Y., Li, H., Du, W., Zhang, H., et al.: How far north did the African Monsoon fringe expand during the African Humid Period? Insights from Southwest Moroccan speleothems, Geophysical Research Letters, 46, 14 093–14 102, https://doi.org/10.1029/2019gl084879, 2019.

Shi, X. and Lohmann, G.: Simulated response of the mid-Holocene Atlantic meridional overturning circulation in ECHAM6-FESOM/MPIOM, Journal of Geophysical Research: Oceans, 121, 6444–6469, https://doi.org/10.1002/2015JC011584, 2016.

Shi, X., Werner, M., Pausata, F. S., Liu, J., D'Agostino, R., Hu, Y., Yang, H., Wang, H., Yang, C., and Lohmann, G.: Climate-dependency of impact of increased carbon dioxide on African monsoon rainfall: Insights from model simulations, Geophysical Research Letters, 52, e2024GL112 717, https://doi.org/10.1029/2024GL112717, 2025.

Sidorenko, D., Rackow, T., Jung, T., Semmler, T., Barbi, D., Danilov, S., Dethloff, K., Dorn, W., Fieg, K., Gößling, H. F., et al.: Towards multi-resolution global climate modeling with ECHAM6-FESOM. Part I: model formulation and mean climate, Climate Dynamics, 44, 757–780, https://doi.org/10.1007/s00382-014-2290-6, 2015.

Sidorenko, D., Goessling, H. F., Koldunov, N., Scholz, P., Danilov, S., Barbi, D., Cabos, W., Gurses, O., Harig, S., Hinrichs, C., et al.: Evaluation of FESOM2. 0 coupled to ECHAM6.3: preindustrial and HighResMIP simulations, Journal of Advances in Modeling Earth Systems, 11, 3794–3815, https://doi.org/10.1029/2019ms001696, 2019.

Stouffer, R., Manabe, S., and Bryan, K.: Interhemispheric asymmetry in climate response to a gradual increase of atmospheric CO2, Nature, 342, 660–662, https://doi.org/10.1038/342660a0, 1989.

Vernet, R.: Climate During the Late Holocene in the Sahara and the Sahel: Evolution and Consequences on Human Settlement, pp. 47–63, Springer US, Boston, MA, ISBN 978-0-306-47547-4, https://doi.org/10.1007/0-306-47547-2_4, 2002.

Wallace, J. M. and Hobbs, P. V.: Atmospheric Science, Edition 2, Academic Press, New York, ISBN 978-0-12-732951-2, https://doi.org/10.1016/c2009-0-00034-8, 2006.

Wang, P. X., Wang, B., Cheng, H., Fasullo, J., Guo, Z., Kiefer, T., and Liu, Z.: The global monsoon across time scales: Mechanisms and outstanding issues, Earth-Science Reviews, 174, 84–121, https://doi.org/10.1016/j.earscirev.2017.07.006, 2017.

Watrin, J., Lézine, A.-M., and Hély, C.: Plant migration and plant communities at the time of the "green Sahara", Comptes Rendus. Géoscience, 341, 656–670, https://doi.org/10.1016/j.crte.2009.06.007, 2009.

Wen, Q., Liu, Z., Liu, J., Clemens, S., Jing, Z., Wang, Y., Lv, G., Yan, M., Ning, L., Yuan, L., et al.: Contrasting responses of Indian summer monsoon rainfall and Arabian Sea upwelling to orbital forcing, Communications Earth & Environment, 5, 409, https://doi.org/10.1038/s43247-024-01572-8, 2024.

Wigley, T.: Relative contributions of different trace gases to the greenhouse effect, Climate Monitor, 16, 14–28, https://research-portal.uea.ac.uk/en/publications/relative-contributions-of-different-trace-gases-to-the-greenhouse/, 1987.

Zhang, H., Ma, X., Zhao, S., and Kong, L.: Advances in research on the ITCZ: Mean position, model bias, and anthropogenic aerosol influences, Journal of Meteorological Research, 35, 729–742, https://doi.org/10.1007/s13351-021-0203-2, 2021.

Zhang, Z., Jansen, E., Sobolowski, S. P., Otterå, O. H., Ramstein, G., Guo, C., Nummelin, A., Bentsen, M., Dong, C., Wang, X., et al.: Atmospheric and oceanic circulation altered by global mean sea-level rise, Nature Geoscience, 16, 321–327, https://doi.org/10.1038/s41561-023-01153-y, 2023.

Zhao, Y., Braconnot, P., Marti, O., Harrison, S., Hewitt, C., Kitoh, A., Liu, Z., Mikolajewicz, U., Otto-Bliesner, B., and Weber, S.: A multi-model analysis of the role of the ocean on the African and Indian monsoon during the mid-Holocene, Climate Dynamics, 25, 777–800, https://doi.org/10.1007/s00382-005-0075-7, 2005.

Zhou, P., Lu, Z., Keskinen, J.-P., Zhang, Q., Lento, J., Bian, J., van Noije, T., Le Sager, P., Kerminen, V.-M., Kulmala, M., et al.: Simulating dust emissions and secondary organic aerosol formation over northern Africa during the mid-Holocene Green Sahara period, Climate of the Past, 19, 2445–2462, https://doi.org/10.5194/cp-19-2445-2023, 2023.